A System Identification Approach to Modeling of Wave Propagation in Pavements

Roland Hostettler, Magnus Lundberg Nordenvaad, and Wolfgang Birk

DOI:
10.3182/20120711-3-BE-2027.00107

A System Identification Approach to Modeling of Wave Propagation in Pavements ⋆

Roland Hostettler * **Magnus Lundberg Nordenvaad** **
Wolfgang Birk *

* *Luleå University of Technology, Division of Systems and Interaction, Luleå, Sweden (e-mail: {rolhos,wolfgang}@ltu.se)*
** *Uppsala University, Division of Systems and Control, Uppsala, Sweden (e-mail: magnus.lundberg-nordenvaad@it.uu.se)*

Abstract: In this paper, modeling of the pavement as a wave propagation medium and estimation of the corresponding model parameters is approached from a system identification perspective. A model based on the physical background is proposed and the corresponding parameters are then estimated from measurement data. In order to achieve the latter, two estimators are proposed, their performance evaluated, and then applied to the measurement data. It is found that the proposed methods are applicable and the results show that different eigenmodes of the structure are excited.

Keywords: Wave guides, Physical models, Mode analysis, Estimators, Non-parametric identification

1. INTRODUCTION

Recent development of new methods for traffic counting showed that it is possible to measure and process waves on the road surface originating from vehicles in order to estimate vehicle and traffic parameters (Hostettler et al., 2010; Bajwa et al., 2011). Even though the feasibility was shown, little is known about the exploited phenomenon. To take this approach further, it is thus of vital importance to understand the physical background. As a first step in this process, it is therefore of interest to understand how the waves propagate in the pavement.

The analysis of wave propagation in pavements is also used in non-destructive testing (NDT) of pavement structures. These methods normally aim at backcalculating pavement parameters, for example for wear prediction and maintenance. Different approaches are in use to date (Goktepe et al., 2006; Goel and Das, 2006) and, for example, Ryden et al. (2004) have pushed the field forward in recent years. Looking at the problem, it is easy to understand that this can be seen as a typical application of system identification. Thus, it is the objective of this paper to examine it as a such. The novelty is that the problem is put into a statistical framework and good properties of the estimated parameters in this sense are sought.

This paper is organized as follows. First, a short recap of wave propagation theory in the road is given in Section 2 and the physical model chosen is explained. This is followed by the description of the system identification experiments and signal analysis in Section 3. Then, two estimators, one for the attenuation coefficients and one for the phase velocity together with their evaluation are proposed in Section 4. Finally, the evaluation of applying the developed tools to the measurement data is given in Section 5.

⋆ Financial support from *Gunnar och Märtha Bergendahls Stiftelse*, GEVEKO AB and the Swedish Governmental Agency for Innovation Systems (VINNOVA) are hereby gratefully acknowledged.

2. WAVE PROPAGATION

In general, wave propagation in solid (and fluid) media can pose all kind of problems ranging from trivial to very difficult. The level of complexity depends heavily on the mechanical structure in which the waves propagate. For a road that is composed of a layered subgrade with an asphalt concrete plate on top (Figure 1), this becomes a problem of waves in a supported plate. These kind of waves have been studied to some extent and the most fundamental work was done by Lamb (1917) who laid the fundamentals for Lamb wave theory. An extensive coverage of the theory is beyond the scope of this paper, thus only the most important principles are captured here. The interested reader is referred to, for example, the work by Rose (1999).

Lamb waves can be seen as the product of waves reflected at the plate boundaries. The original waves induced are reflected at the top and bottom of the plate multiple times and due to the superposition new wave modes emerge. The resulting modes can be divided into three main categories: Symmetric (S), antisymmetric (A), and shear-horizontal (SH) modes. An infinite number of these modes exists. The S- and A-modes have their particle motion mostly in the out-of-plane and radial in-plane directions whereas SH-modes have their particle motion in the tangential in-plane direction.

One of the most important properties for characterizing waves is the phase velocity. It generally is a function of frequency (dispersive waves) and can by calculated by

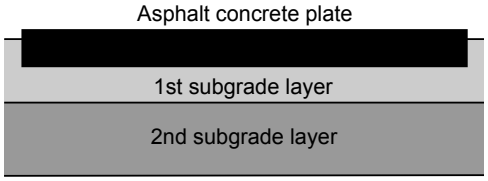

Fig. 1. Illustration of a typical road cross-section consisting of an asphalt concrete plate on top and one or more subgrade layers.

using the Lamb wave dispersion relation (Rose, 1999) if the material parameters are known. The phase shift added for a wave traveling the distance r can be described as

$$\varphi_r = -\frac{\omega r}{c_p(\omega)}. \tag{1}$$

Adding the phase shift φ_0 between the excitation and measurement (e.g. phase between force and acceleration), the phase angle becomes

$$\angle H(r, i\omega) = \varphi_0 - \frac{\omega r}{c_p(\omega)} \tag{2}$$

where $H(r, i\omega)$ is the distance-dependent transfer function describing the wave propagation.

Furthermore, Lamb waves in pavements are also subject to damping when propagating away from the source. Using the asymptotic approximation of the Hankel function that is obtained from the solution of classical plate theory (Doyle, 1997), the magnitude is obtained as

$$|H(r, i\omega)| = \frac{A(\omega)}{\sqrt{r}} e^{-\beta(\omega) r}. \tag{3}$$

Combining (2) and (3), the model for the propagation path becomes

$$H(r, i\omega) = \frac{A}{\sqrt{r}} e^{-\beta r} e^{i\left(\varphi_0 - \frac{\omega r}{c_p}\right)} \tag{4}$$

where the dependency of A, β, and c_p on ω has been dropped for brevity.

3. EXPERIMENTS

In order to use the theory introduced in the previous section and to estimate the model parameters, system identification experiments on the road were conducted. This section describes the experimental setup used to gather the necessary data and provides a first analysis of the data. The parameter estimation is discussed in Section 4.

3.1 Experiment Setup

The experiment setup used is illustrated in Figure 2. The pavement was excited using a sledge hammer and the response was measured with an accelerometer. The excitation force (input) was measured with a force transducer mounted on the sledge hammer. The distance between the excitation (hammer impact point) and the sensor was varied in 0.5m-steps from 0.5m up to 6m yielding $M = 12$ spatially separated measurement points. At each distance, the experiment was repeated $K = 10$ times. Note that once the experiment is set up, the time to conduct the measurements is given by $K \cdot M$. For a fixed experiment time, this results in a trade-off between spatial information which contributes to the accuracy of the parameters of interest and averaging of the individual transfer functions as it will be shown in the following sections.

The excitation produced by the hammer is a rather sharp pulse. Clearly, this is not an ideal excitation for the purpose of system identification as the amplitude and frequency content cannot be controlled very well. However, using more structured excitation signals such as multisines (Pintelon and Schoukens, 2001) is more difficult. For this purpose, shakers attached to the ground could be used (see, e.g. Goel and Das (2006)). Two obvious challenges with that are the transmission of the force into the structure and the limited dynamics of the shaker.

Furthermore, note that the excitation is mostly normal to the surface and thus, the response measured in the same orientation will carry the most information.

3.2 Input and Output Signal Analysis

The force created by the hammer exceeds several kN and thus, a lot of energy is injected to excite the pavement. The output $y^{(d)}[n]$ (the superscript (d) denotes the measurement direction x, y, or z) on the other hand is a rather weak acceleration and the following measurement model is assumed

$$\begin{aligned} x[n] &= u[n] \\ y^{(d)}[n] &= h_0[n] * u[n] + w[n] \end{aligned} \tag{5}$$

where $u[n]$ is the excitation signal, $h_0[n]$ the true impulse response, $w[n] \sim \mathcal{N}(0, \sigma_w^2)$, and $*$ denotes the convolution.

The measured signals are then transformed to the frequency domain to perform further analysis. The unitary Fast Fourier Transform (scaling $1/\sqrt{N}$) is used to obtain the Fourier coefficients and the first order *diff*-window (Schoukens et al., 2006)

$$X_{k,r_m}(i\omega_{l+0.5}) = X_{k,r_m}(i\omega_{l+1}) - X_{k,r_m}(i\omega_l) \tag{6}$$

is applied to reduce leakage for both the input and output signals. Note that the index l is omitted for better readability.

Figure 3 shows an example of the input and output signal amplitude spectra for $r = 2$m. It can be seen that the input's half-power bandwidth (blue) is approximately 330Hz and at 800Hz it has decayed by more than 20dB on average.

The output spectra show that mainly two frequency ranges are excited. The first between approximately 300Hz and 1kHz and the second around 4kHz to 5kHz. Comparing that to the excitation, one can see that both of these two regions are weakly excited. Thus, it can be concluded that new modes were excited.

When comparing the amplitude of the different orientations of the sensor (direction of particle motion), it is observed that the out-of-plane motion (z) is predominant,

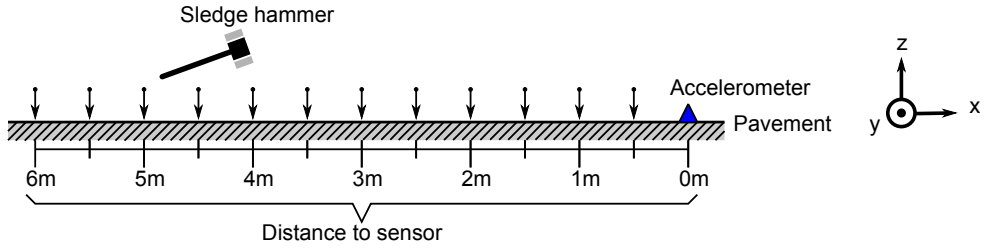

Fig. 2. Illustration of the experiment setup showing the excitation (hammer) and the sensor location together with the coordinate system used.

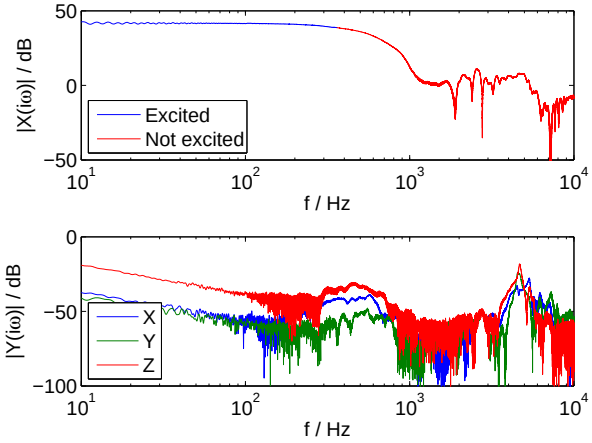

Fig. 3. Examples of measured input- (top) and output (bottom) specta for $r = 2$m.

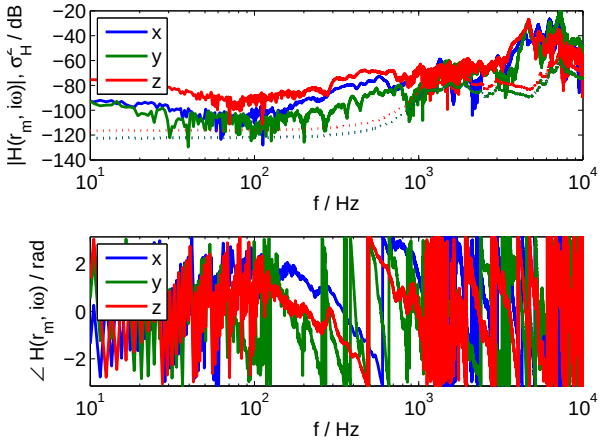

Fig. 4. Magnitude (top; solid), phase (bottom), and variance (top; dotted) of the transfer function obtained from the experimental data for $r = 2$m.

followed by the radial in-plane motion (x) and the tangential in-plane motion (y).

3.3 Non-Parametric Transfer Function

For each of the $K = 10$ input-output pairs at distance r_m, the individual transfer function

$$\hat{H}_k(r_m, i\omega) = \frac{Y_{k,r_m}(i\omega)}{X_{k,r_m}(i\omega)} = H_0(r_m, i\omega) + \frac{W(i\omega)}{X_{k,r_m}(i\omega)} \quad (7)$$

is estimated. For simplicity, we assume that $\boldsymbol{W}(i\omega)$ is Gaussian distributed according to $\boldsymbol{W}(i\omega) \sim \mathcal{CN}(0, 2\sigma_w^2 \boldsymbol{I})$ (Kay, 1993). Due to the windowing in (6), this is not exactly true. However, for all practical purposes the assumption is accurate enough. For $\tilde{W}(i\omega) = W(i\omega)/X_{k,r_m}(i\omega)$, the noise becomes $\tilde{\boldsymbol{W}}(i\omega) \sim \mathcal{CN}(0, \boldsymbol{C}_{\tilde{W}_k})$ with the elements of the covariance matrix $\boldsymbol{C}_{\tilde{W}_k}$ as

$$\left[\boldsymbol{C}_{\tilde{W}_k}\right]_{pq} = \begin{cases} 2\sigma_w^2 (X_{k,r_m}(i\omega_p) X_{k,r_m}^*(i\omega_q))^{-1} & \text{p} = \text{q} \\ 0 & \text{p} \neq \text{q} \end{cases} \quad (8)$$

and thus $\hat{\boldsymbol{H}}_k(r_m, i\omega) \sim \mathcal{CN}\left(\boldsymbol{H}_0(r_m, i\omega), \boldsymbol{C}_{\tilde{W}_k}\right)$.

For each distance r_m, the final transfer function estimate is the weighted average over all realizations, i.e.

$$\hat{\boldsymbol{H}}(r_m, i\omega) = \left(\sum_{k=1}^{K} \boldsymbol{C}_{\tilde{W}_k}^{-1}\right)^{-1} \left(\sum_{k=1}^{K} \boldsymbol{C}_{\tilde{W}_k}^{-1} \hat{\boldsymbol{H}}_k(r_m, i\omega)\right) \quad (9)$$

and the covariance is

$$\boldsymbol{C}_{\hat{H}} = \text{cov}\left(\hat{\boldsymbol{H}}(r_m, i\omega)\right) = \left(\sum_{k=1}^{K} \boldsymbol{C}_{\tilde{W}_k}^{-1}\right)^{-1}. \quad (10)$$

An example of a transfer function calculated according to (9) and its variance (10) is shown in Figure 4.

4. PARAMETER ESTIMATION

Based on the model introduced in Section 2 and the measurements model in Section 3, two estimators, one for the attenuation coefficients and one for the phase velocity, are proposed and evaluated in this section.

4.1 Attenuation Coefficients

Assuming the model in (7), it is known (Papoulis, 1984) that the magnitude $z_m = |\hat{H}(r_m, i\omega_l)|$ is distributed according to the Rice distribution

$$p(z_m; \boldsymbol{\theta}) = \frac{2z_m}{\sigma_m^2} e^{-\frac{1}{\sigma_m^2}(z_m^2 + z_{0,m}^2(\boldsymbol{\theta}))} I_0\left(\frac{2z_{0,m}(\boldsymbol{\theta}) z_m}{\sigma_m^2}\right) \quad (11)$$

where $I_0(x)$ is the modified Bessel function, $\boldsymbol{\theta} = [A \ \beta]^T$ the parameter vector, and $z_0(\boldsymbol{\theta}) = \frac{A}{\sqrt{r}} e^{-\beta r}$ according to (3). The variance σ_m^2 is given by $\left[\boldsymbol{C}_{\hat{H}}\right]_{ll}$ for $\boldsymbol{C}_{\hat{H}}$ as in (10).

The log-likelihood function for $\boldsymbol{z} = [z_1 \; z_2 \; \dots \; z_M]^T$ is then given by

$$\ln(p(\boldsymbol{z};\boldsymbol{\theta})) = \sum_{m=1}^{M} \ln\left(\frac{2}{\sigma_m^2}\right) + \ln\left(I_0\left(\frac{2z_{0,m}(\boldsymbol{\theta})z_m}{\sigma_m^2}\right)\right) + \ln(z_m) - \frac{1}{\sigma_m^2}\left(z_m^2 + z_{0,m}^2(\boldsymbol{\theta})\right). \tag{12}$$

Note that the arguments to the Bessel function are generally large in this case and thus, the asymptotic approximation of first order

$$I_0(x) \approx \frac{1}{\sqrt{2\pi x}} e^x \tag{13}$$

can be used (Abramowitz and Stegun, 1964) instead. The approximated log-likelihood function then becomes

$$\ln(p(\boldsymbol{z};\boldsymbol{\theta})) \approx \sum_{m=1}^{M} \ln\left(\frac{1}{\sqrt{\pi\sigma_m^2}}\right) + \ln\left(\sqrt{\frac{z_m}{z_{0,m}(\boldsymbol{\theta})}}\right) - \frac{1}{\sigma_m^2}\left(z_m - z_{0,m}(\boldsymbol{\theta})\right)^2 \tag{14}$$

No closed form solution that maximizes (14) can be found. Thus, a numerical procedure has to be employed in order to solve

$$\hat{\boldsymbol{\theta}}_{ML} = \underset{\boldsymbol{\theta}}{\operatorname{argmax}} \ln(p(\boldsymbol{z};\boldsymbol{\theta})) \tag{15}$$

A good starting point for this can be obtained by letting

$$\tilde{\boldsymbol{z}} = \ln\left(\sqrt{\boldsymbol{r}}\boldsymbol{I}\boldsymbol{z}\right) = \underbrace{\begin{bmatrix} 1 & r_1 \\ \vdots & \vdots \\ 1 & r_m \end{bmatrix}}_{H} \tilde{\boldsymbol{\theta}} + \boldsymbol{e}$$

and solving the corresponding linear problem with $\tilde{\boldsymbol{\theta}} = [\ln(A) \; \beta]^T$. Note that $\boldsymbol{e}$ is not Gaussian and thus, the solution is not the ML solution.

From (12), the components of the Fisher information matrix can be calculated as

$$[\boldsymbol{I}(\boldsymbol{\theta})]_{11} = -\sum_{m=1}^{M} \frac{4z_{0,m}^2(\boldsymbol{\theta})}{A^2\sigma_m^4}\left(z_{0,m}^2(\boldsymbol{\theta}) - \mathcal{K}\right) \tag{16a}$$

$$[\boldsymbol{I}(\boldsymbol{\theta})]_{12} = -\sum_{m=1}^{M} \frac{4z_{0,m}^2(\boldsymbol{\theta})r_m}{A\sigma_m^4}\left(\mathcal{K} - z_{0,m}^2(\boldsymbol{\theta})\right) \tag{16b}$$

$$[\boldsymbol{I}(\boldsymbol{\theta})]_{21} = [\boldsymbol{I}(\boldsymbol{\theta})]_{12} \tag{16c}$$

$$[\boldsymbol{I}(\boldsymbol{\theta})]_{22} = -\sum_{m=1}^{M} \frac{4z_{0,m}^2(\boldsymbol{\theta})r_m^2}{\sigma_m^4}\left(z_{0,m}^2(\boldsymbol{\theta}) - \mathcal{K}\right) \tag{16d}$$

and the Cramér-Rao Lower Bound (CRLB) of the covariance matrix for $\hat{\boldsymbol{\theta}}$ is then $\boldsymbol{C}_{\hat{\boldsymbol{\theta}}} \geq \boldsymbol{I}(\boldsymbol{\theta})^{-1}$. The constant $\mathcal{K}$ in (16) is given by

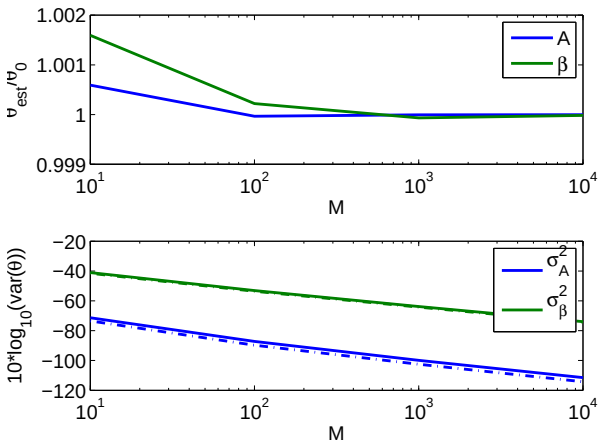

Fig. 5. Evaluation of the attenuation coefficients estimator. The estimator is asymptotically unbiased with very little initial bias (top) and very close to the Cramér-Rao Lower Bound (bottom).

$$\mathcal{K} = \mathrm{E}\left\{ z_m^2 \frac{I_1^2\left(\frac{2z_m z_{0,m}(\boldsymbol{\theta})}{\sigma_m^2}\right)}{I_0^2\left(\frac{2z_m z_{0,m}(\boldsymbol{\theta})}{\sigma_m^2}\right)} \right\} \tag{17}$$

with z_m distributed as given by (11). Unfortunately, (17) cannot be evaluated analytically and has to be calculated numerically, possibly using numerical methods such as the continued fraction method (Lentz, 1976) to evaluate the ratio of the Bessel functions. Note that the inequality $I_1(x)/I_0(x) < 1$ gives an upper bound on $\mathcal{K}$ and thus a lower bound on the CRLB. Similarly, inequalities for the lower bound of $\mathcal{K}$ exist (Laforgia and Natalini, 2010). However, they do not simplify the problem significantly.

In order to evaluate the performance of the estimator, 10^4 simulations with $\boldsymbol{\theta}_0 = [0.01 \; 0.1]^T$, $\sigma_m^2 = 10^{-7}$, and $M = \{10^1, 10^2, 10^3, 10^4\}$ points between $r = 10\mathrm{m}/M$ and $r = 10\mathrm{m}$ were performed. Figure 5 (top) shows the ratios $\hat{A}/A_0$ and $\hat{\beta}/\beta_0$. It can be seen that the estimator is asymptotically unbiased for both parameters as the ratios approach 1. Furthermore, the bias is very low for few measurements (less than 0.1% at maximum). The variances together with the CRLBs are shown in the lower part of Figure 5.

4.2 Phase Velocity

Using (4) and (7), the measured phase φ_m is given as

$$\varphi_m = \varphi_0 - \frac{\omega r_m}{c_p} + \epsilon \tag{18}$$

where $\epsilon \sim \mathcal{U}[-\pi, \pi]$ is the phase noise. Note that phase unwrapping (along r) could be used in order to recover the true value of φ_m. In this case, the distance Δr between r_m and r_{m+1} should follow $\Delta r < c_p/f$ in order to avoid ambiguity. This is a problem in itself since c_p is the variable that is to be estimated. The problem can be treated by assuming a c_p in the order of the true phase velocity and designing the experiment accordingly. (18) can be reformulated to

$$\tilde{\varphi}_m = \tilde{\varphi}_0 - \frac{\omega}{c_p} + \tilde{\epsilon} \tag{19}$$

where $\tilde{\varphi}_m = \varphi_m / r_m$, $\tilde{\varphi}_0 = \varphi_0 / r_m$, and $\tilde{\epsilon} = \epsilon / r_m$. The PDF for $\tilde{\varphi}$ then becomes

$$p(\tilde{\varphi}_m; \theta) = \begin{cases} \dfrac{r_m}{2\pi} & \tilde{\varphi}_0 - \dfrac{\omega}{c_p} - \dfrac{\pi}{r_m} < \tilde{\varphi}_m < \tilde{\varphi}_0 - \dfrac{\omega}{c_p} + \dfrac{\pi}{r_m} \\ 0 & \text{otherwise} \end{cases}. \tag{20}$$

In this case, $\theta = c_p$ and φ_0 is known. From (20), the joint PDF for $\tilde{\boldsymbol{\varphi}} = [\tilde{\varphi}_1 \ \tilde{\varphi}_2 \ \dots \ \tilde{\varphi}_M]^T$ is

$$\begin{aligned} p(\tilde{\boldsymbol{\varphi}}; \theta) = \prod_{m=0}^{M} \frac{r_m}{2\pi} \, \mathrm{u}\left(\min\left(\tilde{\boldsymbol{\varphi}} - \tilde{\boldsymbol{\varphi}}_0 + \pi \tilde{\boldsymbol{r}} \right) + \frac{\omega}{c_p} \right) \\ \cdot \, \mathrm{u}\left(- \max\left(\tilde{\boldsymbol{\varphi}} - \tilde{\boldsymbol{\varphi}}_0 - \pi \tilde{\boldsymbol{r}} \right) - \frac{\omega}{c_p} \right) \end{aligned} \tag{21}$$

where $\tilde{\boldsymbol{r}} = [1/r_1 \ 1/r_2 \ \dots \ 1/r_M]$ and $\mathrm{u}(x)$ is the unit step function. The Neyman-Fisher Factorization (Kay, 1993) is applied to (21) in order to obtain the two sufficient statistics

$$\boldsymbol{T}(\tilde{\boldsymbol{\varphi}}) = \begin{bmatrix} T_1(\tilde{\boldsymbol{\varphi}}) \\ T_2(\tilde{\boldsymbol{\varphi}}) \end{bmatrix} = \begin{bmatrix} \min\left(\tilde{\boldsymbol{\varphi}} - \tilde{\boldsymbol{\varphi}}_0 + \pi \tilde{\boldsymbol{r}} \right) \\ \max\left(\tilde{\boldsymbol{\varphi}} - \tilde{\boldsymbol{\varphi}}_0 - \pi \tilde{\boldsymbol{r}} \right) \end{bmatrix}. \tag{22}$$

By letting $T_3 = (T_1 + T_2)/2$, it can be shown that

$$\mathrm{E}\{T_3\} = -\frac{\omega}{c_p} \tag{23}$$

and thus $\hat{k} = -T_3$ is an unbiased estimator for the wavenumber $k = \omega / c_p$. Unfortunately, the expected value of the transformed estimator

$$\hat{c}_p = -\frac{\omega}{T_3} \tag{24}$$

is biased (the proof is omitted here for brevity). However, the bias scales quickly as M increases and (24) can be considered a viable estimator. Since (21) is non-differentiable, the CRLB for $\hat{c}_p$ can not be established.

The estimator performance is evaluated by running 10^4 simulations with $\theta_0 = 1'000\mathrm{m/s}$ and $\theta_0 = 10'000\mathrm{m/s}$ for $M = \{10^1, 10^2, 10^3, 10^4\}$ samples of the phase at M different distances. The results are shown in Figure 6. As predicted, the estimator is biased for low numbers of samples but the bias is very small and decreases rapidly.

5. RESULTS

The estimators proposed in the preceding section were applied to the system identification experiments as described in Section 3. According to the theory presented, the estimation of the damping coefficients and phase velocity is done for each frequency individually using all the $M = 12$ spatial measurement.

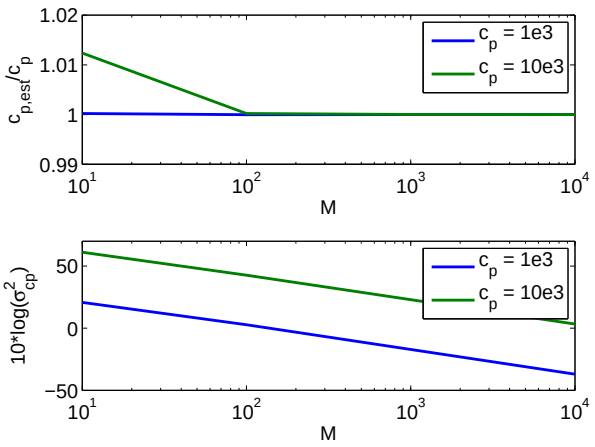

Fig. 6. Simulation results for the phase velocity estimator (24). Top: Ratio between the estimated value and the true value $\hat{c}_p / c_p$. Bottom: Variance of $\hat{c}_p$.

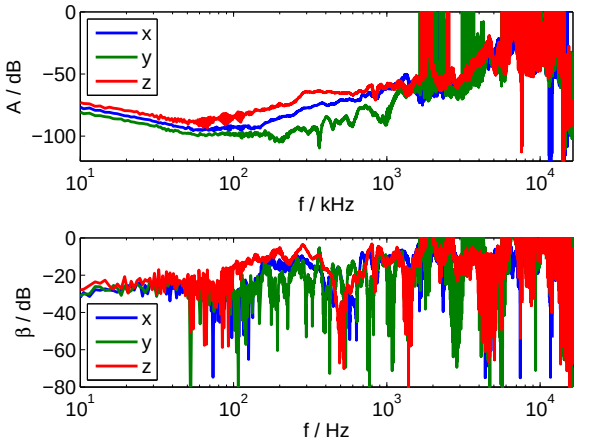

Fig. 7. Estimated damping coefficients $\hat{A}(\omega)$ (top) and $\hat{\beta}(\omega)$ (bottom).

5.1 Attenuation Coefficients

The estimated coefficients $\hat{A}$ and $\hat{\beta}$ are shown in Figure 7. Restricting the discussion to the modes identified earlier, it becomes immediately apparent that the attenuation characteristics differ depending on the direction of particle motion. As expected, the y-direction exhibits very high attenuation which can be explained by the little excitability in that direction. Furthermore, the x- and z-directions show similar behavior, especially around 800Hz to 1kHz.

Comparing the two coefficients A and β, not much similarity can be discovered in the excited ranges. A connection between the two is not apparent.

5.2 Phase Velocity

Figure 8 shows the results of applying the phase velocity estimator (24) to the measurement data. Note that in the shown dispersion curves, points with high residuals were removed in order to improve readability.

When considering the whole measured frequency range, it is seen that besides the excited components around <

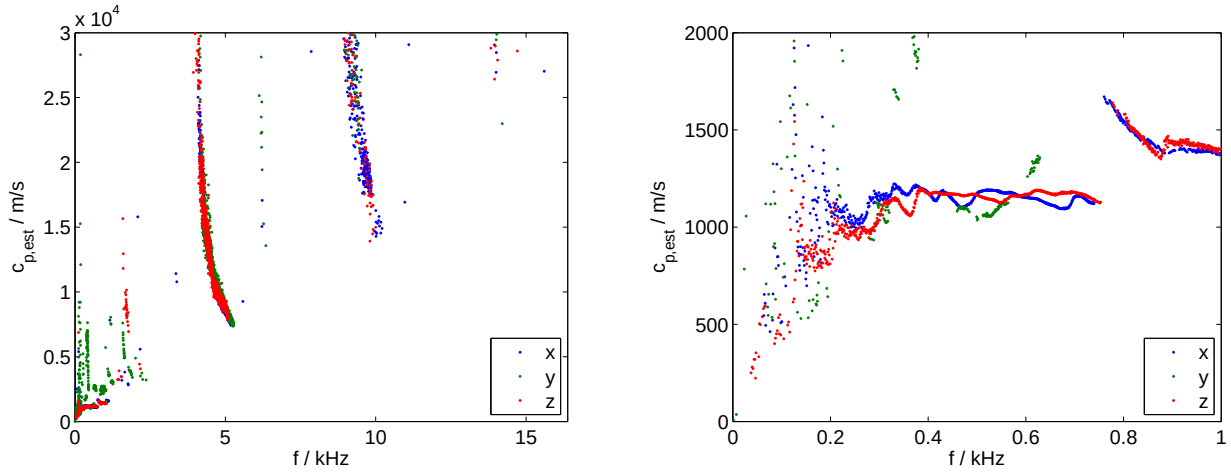

(a) (b)

Fig. 8. Dispersion curves obtained from the estimated phase velocities. (a) Whole measurement range up to 16kHz, and (b) enlargement of the range between 0Hz and 1kHz.

1kHz, the previously identified mode around 4kHz to 5kHz as well as more higher modes are revealed (Figure 8a). The enlargement of the low frequencies in Figure 8b shows that the phase velocity is nearly constant at frequencies below 750Hz. Then, around 750Hz, a jump in phase velocity is encountered. This is very likely to be attributed to a mode change (Rose, 1999).

Two observations can be made when analyzing the differences between the three directions of particle motion. Firstly, the x- and z-directions behave similarly. This is no surprise as the particle motion for the dominating modes is in the radial in-plane and tangential directions (see Section 2). The behavior for the y-axis is different and basically confirms the previous observations. Due to the weak excitation in that direction little is measured. Some residuals might be present because of alignment inaccuracies and reflections at the boundary.

6. CONCLUSION

It was shown how wave propagation parameters from spatio-temporal data obtained from system identification experiments can be estimated. Using a statistical framework, two well-behaved estimators were proposed, evaluated, and applied to the measurement data. Interesting results were obtained from both the attenuation coefficients and the dispersion curves which help to understand the underlying problem better.

Some of the methods presented have to be developed more thoroughly as indicated before. Especially the underlying theory of wave propagation and the chosen approximation contain more information about and connections between the three parameters considered. Clearly, this should be taken into account when developing the proposed methods further.

REFERENCES

Abramowitz, M. and Stegun, I.A. (1964). *Handbook of Mathematical Functions.*

Bajwa, R., Rajagopal, R., Varaiya, P., and Kavaler, R. (2011). In-pavement wireless sensor network for vehicle classification. In *Information Processing in Sensor Networks (IPSN), 2011 10th International Conference on*, 85–96.

Doyle, J.F. (1997). *Wave Propagation in Structures - Spectral Analysis Using Fast Discrete Fourier Transforms.* Springer.

Goel, A. and Das, A. (2006). A brief review on different surface wave methods and their applicability for non-destructive evaluation of pavements. In *2006 Highway Geophysics-NDE Conference*, 337–350.

Goktepe, A.B., Agar, E., and Lav, A.H. (2006). Advances in backcalculating the mechanical properties of flexible pavements. *Advances in Engineering Software*, 37(7), 421–431.

Hostettler, R., Birk, W., and Lundberg Nordenvaad, M. (2010). Feasibility of road vibrations-based vehicle property sensing. *Intelligent Transport Systems, IET*, 4(4), 356–364.

Hostettler, R., Lundberg Nordenvaad, M., and Birk, W. (2012). A system identification approach to modeling of wave propagation in pavements. In *16th IFAC Symposium on System Identification.* Brussels, Belgium.

Kay, S.M. (1993). *Fundamentals of Statistical Signal Processing: Estimation Theory.* Prentice Hall.

Laforgia, A. and Natalini, P. (2010). Some inequalities for modified bessel functions. *Journal of Inequalities and Applications.*

Lamb, H. (1917). On waves in an elastic plate. In *Proceedings of the Royal Society of London*, 114–128.

Lentz, W.J. (1976). Generating Bessel functions in mie scattering calculations using continued fractions. *Appl. Opt.*, 15(3), 668–671.

Papoulis, A. (1984). *Probability, Random Variables, and Stochastic Processes.* McGraw-Hill.

Pintelon, R. and Schoukens, J. (2001). *System Identification: A Frequency Domain Approach.* Wiley-IEEE Press.

Rose, J.L. (1999). *Ultrasonic Waves in Solid Media.* Cambridge University Press.

Ryden, N., Park, C.B., Ulriksen, P., and Miller, R.D. (2004). Multimodal approach to seismic pavement testing. 130(6), 636–645.

Schoukens, J., Rolain, Y., and Pintelon, R. (2006). Leakage reduction in frequency-response function measurements. *IEEE Transactions on Instrumentation and Measurement*, 55.